J Mater Sci (2007) 42:2543–2550
DOI 10.1007/s10853-006-1208-z

Structural and electrical properties of SiO_2–Li_2O–Nb_2O_5 glass and glass-ceramics obtained by thermoelectric treatments

M. P. F. Graça · M. G. Ferreira da Silva · M. A. Valente

Received: 16 November 2005 / Accepted: 6 February 2006 / Published online: 2 January 2007

Abstract Glass and glass-ceramics with the molar composition of $60SiO_2$–$30Li_2O$–$10Nb_2O_5$ (mole %) were studied. Ferroelectric lithium niobate ($LiNbO_3$) nanocrystals were precipitated in the glass matrix trough a thermal treatment, with and without the simultaneous application of an external electric field. The as-prepared sample, yellow and transparent, was heat-treated (HT) at 600 and 650 °C and thermoelectric treated (TET) at 600 °C. The applied electric fields were the following ones: (i) 5×10^4 V/m; (ii) 1×10^5 V/m. Differential thermal analysis (DTA), X-ray diffraction (XRD), scanning electron microscopy (SEM), Raman and dielectric spectroscopies were used to investigate the glass samples properties.

The $LiNbO_3$ crystalline phase was detected in the 650 °C HT sample and in the 600 °C TET samples. The presence of an external electric field, during the heating process, promotes the glass crystallization at lower temperatures. In the TET samples, the surface crystallization of the cathode and the anode are different.

The number and size of the crystallites, in the glass network, dominate the electrical dc behavior while the ac conductivity process is more dependent of the glass matrix structure.

The obtained results reflect the important role carried out by the temperature and the applied electric field in the glass-ceramic structures.

M. P. F. Graça (✉) · M. A. Valente
Physics department (FSCOSD), Aveiro University,
Campus Universitário de Santiago,
Aveiro 3800-193, Portugal
e-mail: mgraca@fis.ua.pt

M. G. Ferreira da Silva
Glass and ceramic engineering department (CICECO),
Aveiro University, 3800-193 Aveiro, Portugal

Introduction

The study of the physical properties of glass-ceramics with ferroelectric crystallites has achieved, in the last years, a considerable amount of interest due to their electrical, dielectrical and electro-optic properties and significant technological applications [1]. Lithium niobate ($LiNbO_3$) is an important ferroelectric material due to its excellent pyroelectrical, piezoelectrical and photorefractive properties [1, 2] and it is actually used for fabrication of active waveguides, modulators, frequency doubler, optical filter and Q-switches for application in integrated optical circuits [3, 4]. This ferroelectric material has a high Curie temperature, T_c = 1210 °C [5]. However, the usual preparation of $LiNbO_3$ crystals, by the Czochralski method, is time consuming, very expensive and with Li deficiency crystals [1, 2, 6]. Glass-ceramics, with the ferroelectric crystal phase, seems to be an interesting alternative due to its relative low preparation time and costs [7, 8].

In the present work it is described the preparation of the $60SiO_2$–$30Li_2O$–$10Nb_2O_5$ (mole %) glass, by the melt-quenching method, and glass-ceramics with and without the application of an electric field during the heat-treatment process (in the text HT denotes heat-treatment and TET the thermoelectric treatment). This composition was chosen because it gives origin to a transparent glass. The SiO_2 was used, as the glass forming oxide, because it does not modify the $LiNbO_3$

lattice [8, 9]. The correlation between the glass-ceramics treatment conditions and their microstructure was the main purpose of this work.

Experimental

Samples preparation

A glass with the molar composition $60SiO_2$–$30Li_2O$–$10Nb_2O_5$ was prepared by the melt-quenching method. This composition enables the formation of a transparent glass suitable for optical applications. The glass was prepared from reagent grade silicon oxide (SiO_2-BDH), lithium carbonate (Li_2CO_3-Merck) and niobium oxide (Nb_2O_5-Merck). The reagents, in the appropriate amounts, were mixed for 1 h, in an agate ball-mixing planetary system. The mixture was heated in a platinum crucible at 700 °C, for 2 h, to remove the CO_2 from the Li_2CO_3, and melted at 1450 °C for 30 min. The molten material was quenched by pouring it into a stainless steel plate, at room temperature, and pressed by another, to obtain flat samples with 10^{-3} m of thickness (approximately). The result was an uncolored and transparent glass. The glass was annealed at 350 °C (during 3 h), to eliminate internal stress, and slowly cooled until room temperature (as-prepared sample).

To obtain the glass ceramics, the as-prepared sample was heat-treated (HT) in air, in a horizontal tubular furnace, at 600 and 650 °C, with a heating rate of 75 °C/h, during 4 h. These temperatures were chosen in agreement with the DTA result of the as-prepared sample, performed in a *Lynseis Aparatus*, in the temperature range of 20–1200 °C, with a heating rate of 5 °C/min and using Al_2O_3 has reference.

The thermoelectric treatments (TET) were performed in an apparatus where the as-prepared sample is between two platinum electrodes, which are connected to a high dc-voltage supply (PS325-Stanford Research System), working between 25 and 2500 V. This apparatus is introduced in a vertical furnace. The as-prepared sample was TET at 600 °C, during 4 h, applying the electric field of 50 kV/m (600B sample) and 100 kV/m (600C sample). 100 kV/m was the higher applied electric field, because when the intensity of the electric field is higher than 100 kV/m dark zones appear in the cathode surface (as observed in the 500 kV/m TET sample).

X-ray diffraction, Raman spectroscopy and scanning electron microscopy

The X-ray diffraction patterns were obtained at room temperature, using bulk samples, in a *Philips X'Pert* system, with a K_α radiation (λ = 1.54056 Å) at 40 kV, and 30 mA, with a step of 0.05 ° and 1 s per step. The Raman spectroscopy, of bulk samples, was carried out in a T64000, Jobin Yvon SPEX spectrometer using an Ar laser (λ = 514.5 nm). The spectra were obtained, in a back-scattering geometry, between 100 and 2000 cm^{-1}. The scanning electron microscopy (SEM) was performed in a *Philips XL 30 system* on the surface and cross section of all samples.

Electrical measurements

For the electrical measurements the opposite sides of the samples were painted with silver paste. The dc electric conductivity (σ_{dc}) was measured with a Keithley electrometer, model 617, as a function of the temperature (80–370 K). The ac conductivity (σ_{ac}) was measured as a function of the temperature (260–300 K), at 1 kHz, using a *Solartron SI 1260, Impedance/gain-phase analyzer*, measuring the real and the imaginary part of the sample impedance ($Z^* = Z'–jZ''$).

The analytical background, used in the electrical data analysis, was as follows:

(a) The *Arrhenius* expression has been used to fit the temperature dependence of the σ_{dc} (Eq. 1) [10]:

$$\sigma_{dc} = \sigma_0 \exp\left(-\frac{E_{a(dc)}}{k_B T}\right) \quad (1)$$

where σ_0 is a pre-exponential factor, $E_{a(dc)}$ the activation energy, k_B the Boltzmann constant and T the temperature.

(b) The relation showed in Eq. 2 was used to calculate the ac conductivity (σ_{ac}).

$$\sigma_{ac} = \omega \varepsilon_0 \varepsilon'' \quad (2)$$

The imaginary part of the complex permittivity (ε'') was obtained using the complex impedance formalism, $Z^* = 1/(\mu\varepsilon^*)$ (where $\mu = j\omega C_0$, ω is the angular frequency, C_0 the admittance of the empty cell and $j = \sqrt{-1}$ [11–14]). In order to normalize the impedance data a Z^*_{rel} was calculated by $Z^*_{rel} = Z^*(A/d)$, where A is the electrode area and d the sample thickness.

The ac activation energy ($E_{a(ac)}$) was achieved using an Arrhenius expression similar to that presented in the Eq. 1.

Results

The DTA of the as-prepared sample revealed the presence of an exothermic peak at 710 °C and an

endothermic peak at 960 °C. The onset of the glass transition temperature is 665 °C. The as-prepared sample was treated at temperatures in agreement with this result. The visual aspect of the 600HT sample is similar to that of the as-prepared sample. The HT at 650 °C turns the sample translucent. The treatment process at 600 °C, with the presence of an external electric field (600B and 600C samples), leads to the formation of a white layer in the sample surface in contact with the platinum positive electrode (Fig. 1-ii). This layer is not observed in the sample surface in contact with the negative electrode (Fig 1-i).

The XRD, presented in Fig. 2, did not reveal the presence of crystalline phases in the 600HT sample. In the 650HT sample was detected the presence of the $LiNbO_3$ and $Li_2Si_2O_5$ crystalline phases (Fig. 2). These crystalline phases were also detected in the 600TET samples (600B and 600C samples). In the Fig. 2 it can be seen that the intensities of the crystalline peaks are different for the both surfaces of TET sample, being higher for the negative surface. It should be point out that, from the 600B to the 600C sample, the XRD peaks intensity decreases. The cathode surface, of the 600C sample, does not present the $Li_2Si_2O_5$ crystalline phase.

The Raman spectra, of all the samples, are presented in Fig. 3. The 870 and 260–265 cm^{-1} Raman bands, observed in all samples, are the only ones detected in the as-prepared and 600HT samples. The 650HT sample spectra show also bands at 690, 630, 439, 370, 334, 280, 239 and 180 cm^{-1}. All these bands, except the 690 cm^{-1} band, are detected in the 600B and 600C TET sample. In the 600C TET sample two new bands, centered at 750 and 119 cm^{-1}, were detected. It must be emphasized that, in the TET samples, the Raman spectra of the anode and cathode surface are different (Fig. 3).

The SEM micrographs of all samples are presented in Fig. 4. For a clearly visualization of the particles different amplifications were used. In the as-prepared sample it was not observed the presence of particles. In the surface and the fracture surface of the HT samples it was observed the presence of particles with dimensions of 0.9–1 μm (600 and 650HT samples—Fig. 4a–c). When the heat-treatment temperature increases the amount of particles increases (Fig. 4).

The presence of an electric field, during the heat-treatment process, promotes the formation, in the sample anode side, of a white layer with a thickness between 50 and 100 μm (600TET samples). In the cathode side another layer, with a thickness of 40–60 μm, was observed (Fig. 4c–positive surface of the 600B sample). The same characteristics were observed in the 600B TET sample. It was also observed, in the region near the positive electrode samples side, a higher number of particles when compared with that of the opposite side. The size of these particles increases, in the TET samples, with the rise of the applied field (Fig. 4d, e). In the 600B sample the particle average size is 1.5 μm, increasing to 3.0 μm in the 600C sample. The number of particles increases, in the fracture surface of these TET samples, with the rise of the applied electric field.

The dc conductivity (σ_{dc}) decreases with the increase of the HT temperature and the rise of the applied electric field (Table 1). Figure 5 presents the σ_{dc} temperature dependence. The dc activation energy of the as-prepared sample, registered in Table 1, is similar to that of the 600HT sample, decreasing in the 650HT sample. The $E_{a(dc)}$ of the 600B TET sample is similar to that of the 600HT sample but decreases in the 600C sample.

The ac conductivity (σ_{ac}), measured at room temperature, shows a maximum for the 600HT sample (Table 1.). When the thermoelectric field value increases the σ_{ac} decreases. The ac activation energy ($E_{a(ac)}$) is, approximately, constant for all the samples (Table 1). The σ_{ac} increases when the measurement temperature increases (Fig. 6).

Discussion

The transparent and yellow as-prepared sample becomes translucent at 650 °C and opaque at 700 °C.

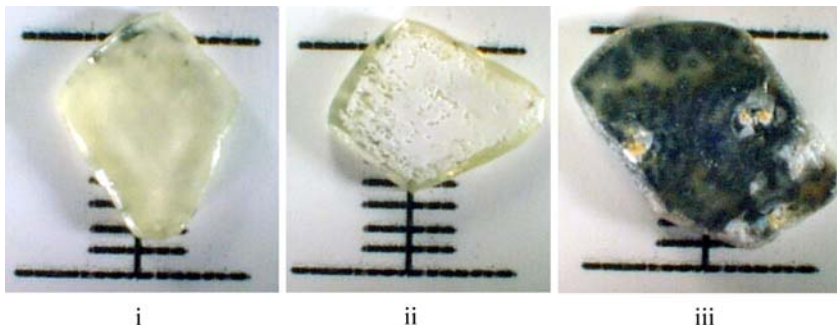

Fig. 1 Photograph of the 600C sample surfaces: i—sample side in contact with the negative electrode; ii—sample side in contact with the positive electrode; iii—the 500 kV/m TET sample at 600 °C (the major scale represents 1 cm)

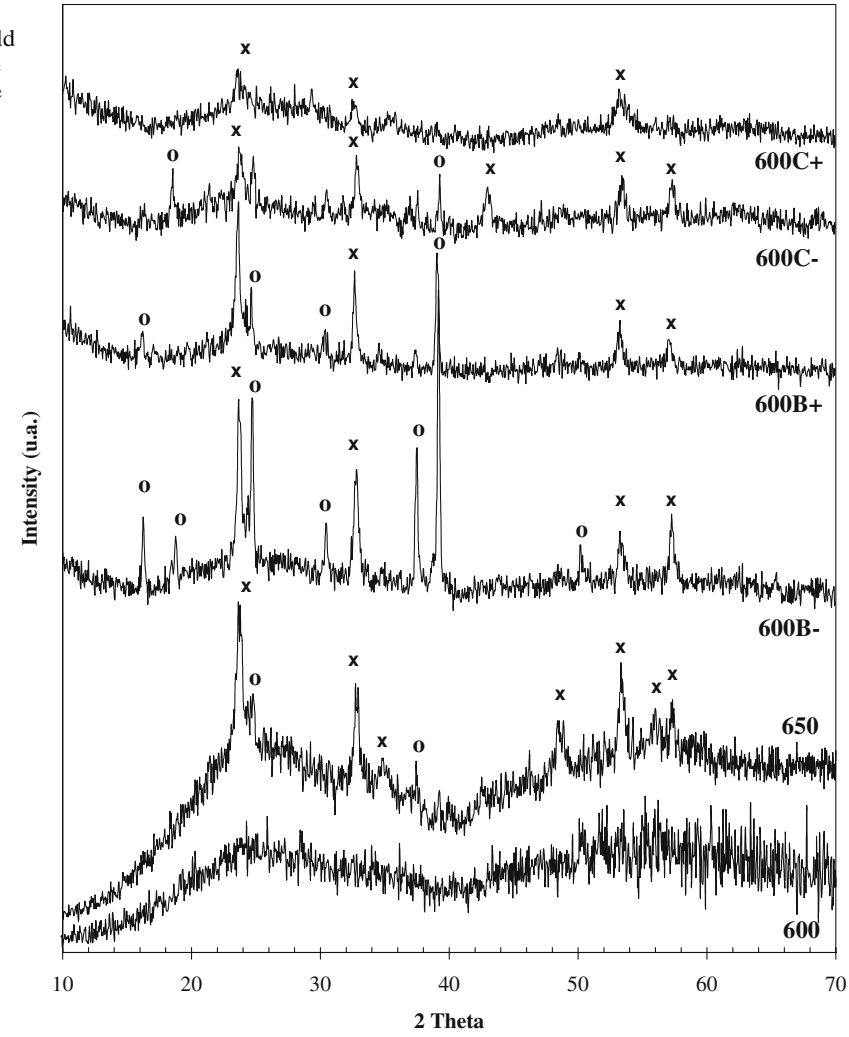

Fig. 2 XRD of the samples treated at 600 and 650 °C with and without an applied electric field (× $LiNbO_3$; ○ $Li_2Si_2O_5$; the "+" represents the sample side treated in contact with the positive electrode and the "–" with the negative side)

These optical characteristics are an indication of the presence of particles embedded in a glass network. Nevertheless, it must be taken in account the number, size and optical characteristics of such particles. If their size and/or number is very small the transparency can be kept. Moreover, if the difference between the refractive indices of the crystallites and the SiO_2-glass matrix is minimum, it will lead to extremely low scattering losses at the glass/crystal interface and the transparency can still remained [15]. This phenomenon is visible in the transparent $Li_2Si_2O_5$ glass-ceramics, containing micro size crystallites [16], which shows a refraction index of ~1.5 [16, 17], closely to the 1.4 of the SiO_2 glass [18]. Thus, it becomes reasonable to assume that the translucent aspect of the 650HT samples is related to the $LiNbO_3$ crystallites, which presents a refraction index of ~2.2 [1]. Moreover, in the 650HT sample the number and intensity of the $LiNbO_3$ XRD peaks is higher than that of the $Li_2Si_2O_5$ peaks (Fig. 2), suggesting a higher number of $LiNbO_3$ crystallites embedded in the glass matrix. However, in the transparent 600HT sample, particles were observed, by SEM, with an average size of 1 μm approximately (Fig. 4a), but were not detected by XRD. This is an indication of the amorphous or incipient crystallization nature of the particles.

In the presence of an external electric field, the 600 °C treated samples becomes translucent and with a white opaque coat in the anode surface side (Fig. 1-ii). In the XRD patterns of these samples (Fig. 2), on the contrary of that obtained for the 600 HT sample (Fig. 2), the presence of crystalline phases was detected. This indicates that the application of an electric field promotes the crystallization of the $LiNbO_3$ and $Li_2Si_2O_3$ phases. It was observed that the use of an electric field higher than 100 kV/m (we have applied 500 kV/m) results in a higher current value that flows in the glass, given origin to dark regions (Fig. 1-iii). The appearance of these dark zones, in accordance with the Kusz [19] and Zeng [20] studies,

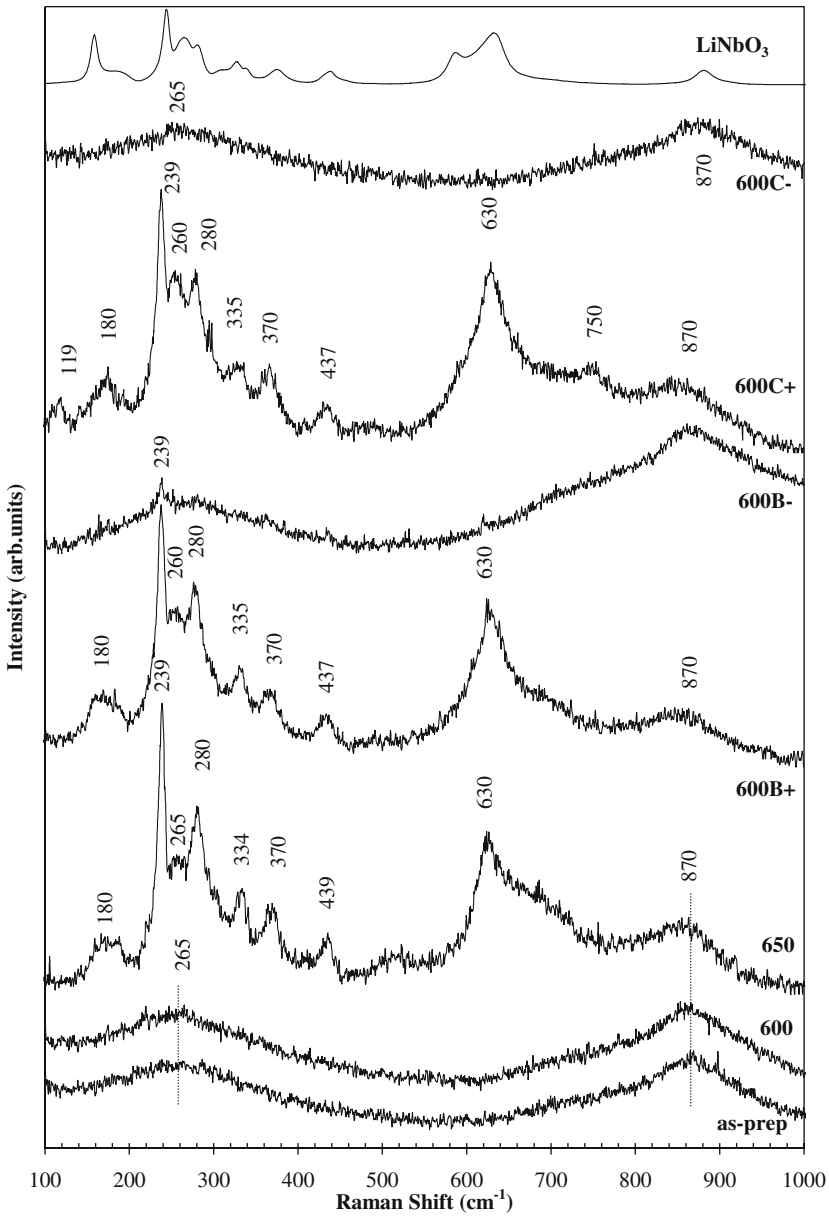

Fig. 3 Raman spectra of all samples (the "+" represents the sample side treated in contact with the positive electrode and the "-" the negative electrode side) and of the commercial $LiNbO_3$

suggest the existence of an oxidation–reduction reaction in the samples, activated by the electric field. In agreement with Zeng et al. [20], the main oxidation–reduction reaction can be summarized in the following equations:

Anodic equation: O^{2-} (glass network) $\rightarrow \frac{1}{2}O_2$ (glass $-$ anode interface) $+ 2e^-$

Cathodic equation: Li^+ (glass network) $+ e^- \rightarrow$ Li (glass - cathode interface)

However, and considering that the glass color change after the TET, other processes can be possible. For example the reduction of Nb^{5+} to a lower oxidation state can occur [20, 21]. In agreement with the study of ionic conduction in silicate glasses, reported by Kusz et al. [19], the presence of dark regions, due to a redox phenomenon, indicates the existence of oxygen ion transport conduction mechanism during the treatment process.

In the TET samples (600B; 600C), the rise of the applied electric field promotes the increase of the particles size (Fig. 4d, e). However, from the Raman spectra (Fig. 3) analysis, it can be assumed that the formation of the $LiNbO_3$ crystalline phase is privileged, in the positive electrode sample zone, due to the detection of the bands at 630, 439–437, 370, 335–334, 280, 265, 239, and 180 cm^{-1}, assigned to the NbO_6 octahedrons vibrations proceeding from $LiNbO_3$ in crystalline form [22–28]. The 750 cm^{-1} band, observed in the anode side

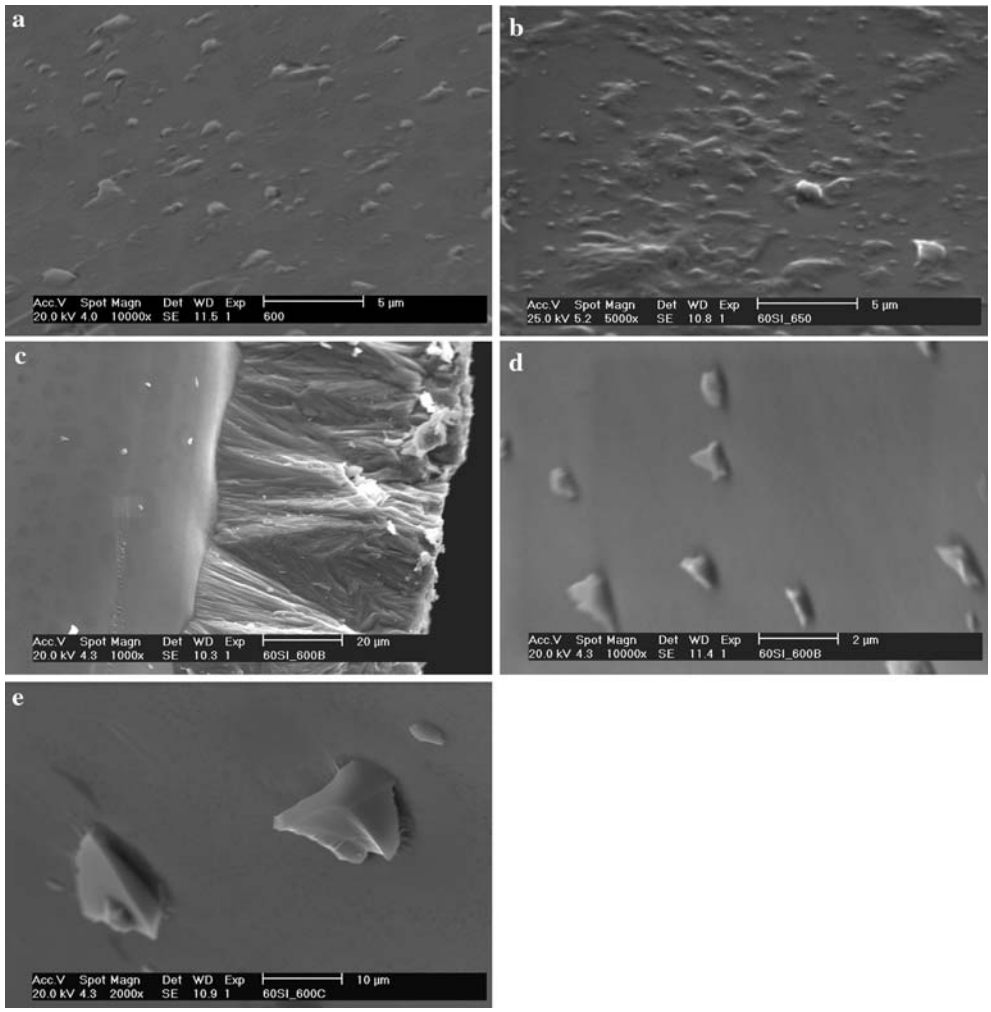

Fig. 4 SEM micrographs of the 600HT (**a**), 650HT (**b**), 600B (**c**—section of the positive electrode sample side), 600B (**d**—cross section) and 600C (**e**—cross section) sample

Table 1 The dc conductivity (σ_{dc}) measured at 300 K, dc activation energy ($E_{a(dc)}$), ac conductivity (σ_{ac}), measured at 300 K and 1 kHz, and ac activation energy ($E_{a(ac)}$) of all samples

Sample	σ_{dc} ($\times 10^{-8}$) [S m^{-1}]	$E_{a(dc)}$ [kJ/mol]	σ_{ac} ($\times 10^{-7}$) [Sm^{-1}]	$E_{a(ac)}$ [kJ/mol]
As-prep	29.4 ± 0.39	58.47 ± 0.66	26.02 ± 0.58	37.37 ± 2.56
600	19.4 ± 0.16	59.03 ± 0.41	31.98 ± 0.71	39.04 ± 1.20
650	1.30 ± 0.31	54.10 ± 0.63	29.01 ± 0.69	38.52 ± 1.62
600B	9.58 ± 0.10	59.83 ± 0.84	22.67 ± 0.58	36.60 ± 1.17
600C	1.98 ± 0.68	55.74 ± 0.61	19.88 ± 0.68	36.22 ± 0.80

of the 600C sample, is attributed to Si–O–Si vibrations [23, 29] of the $Li_2Si_2O_5$ phase. The 119 cm^{-1} band can be assigned to Si–O–Si bending vibrations [23]. The small penetration depth of the incident laser beam can justify the differences between the Raman spectrum of the 600B+ and 600B– samples. Zhang et al. [34] shows that, in amorphous silicate, the 514.5 nm incident laser wavelength leads to a Raman penetration depth of 32.9 nm. These results indicate that the 600B– Raman spectra reflects only the sample surface characteristics. The same happens with the 600C sample.

In the first reports where niobium phases were inserted in glasses, the band between 800 and 940 cm^{-1} was attributed to the NbO_6 isolated octahedrons vibrations [24, 30]. The shift of this band to higher wavenumbers is assigned to the increase of the degree of the octahedrons distortion. However, in recent works, it was suggested that the Raman vibrations in the 870 cm^{-1} region can be due to NbO_4 tetrahedrons [27–29]. Thus, the existence in the Raman spectra, of all the samples, of the 870 cm^{-1} band (Fig. 4), indicates that some Nb ions are, probably, inserted in the glass

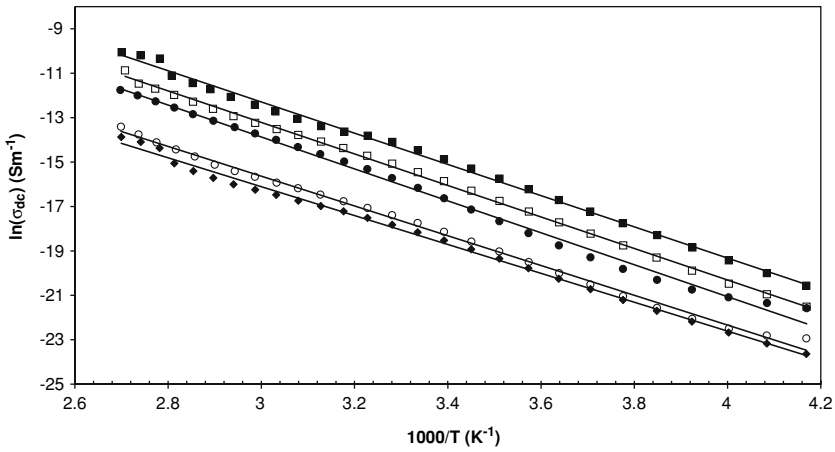

Fig. 5 The σ_{dc} temperature dependence of all samples (■ as-prepared; □ 600; ♦ 650; ● 600B; ○ 600C)

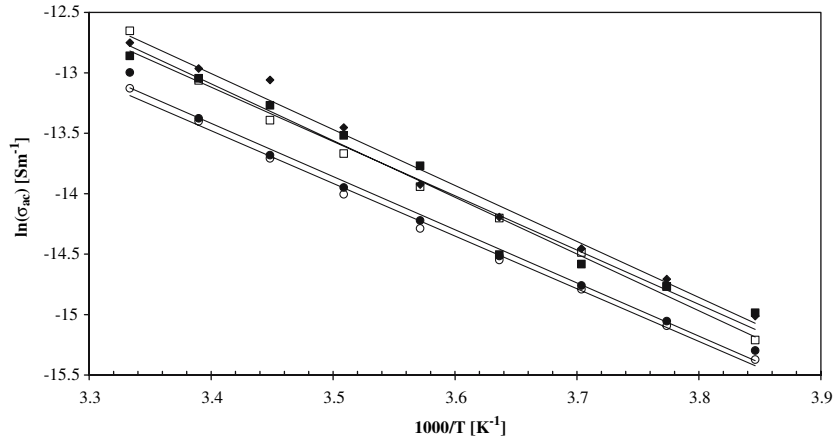

Fig. 6 The σ_{ac} temperature dependence of all samples (■ as-prepared; □ 600; ♦ 650; ● 600B; ○ 600C)

matrix as network formers [9, 23]. However, the inexistence in the Raman spectra, of the 800–850 cm^{-1} bands (Fig. 3), related with the Nb–O–Si non-bridging bonds, indicates that the Nb ions, probably, are not inserted in the glass matrix as network formers. Thus, considering that the niobium ions are inserted, in the silicate glass matrix, as network modifiers, the increase of the HT temperature leads to a decrease of this ions number in the network and consequent increase of the crystallites fraction in the glass. The decrease of σ_{dc} (Table 1), with the increase of the HT temperature, should be related to the crystallites formation because the decrease of free ions in the glass matrix will lead to a diminishing of the conductivity. On the other hand, the high resistivity of the $LiNbO_3$ crystalline phase [1], and the σ~10^{-12} S/m [31], of the $Li_2Si_2O_5$ crystalline phase, at room temperature, will increase the glass-ceramic resistivity. The dc activation energy ($E_{a(dc)}$), obtained through the Arrhenius model ($\ln(\sigma_{dc})$ vs. $1000/T$ - Fig. 5) [11–12, 14], decreases from the 600 to the 650 HT sample (Table 1—the $E_{a(dc)}$ of the as-prepared sample is similar to that of the 600 HT sample). The observed decreasing should be associated to a diminishing of the height of the free energy barriers of the glass matrix quasi-lattice, making the jump process less difficult and therefore contributing to a higher mobility. This indicates that the charge carriers number will dominate this conduction process. The σ_{dc} temperature dependence profile (Fig. 2) is characteristic of a thermally stimulated process. The increase of the conductivity, with the increase of the temperature of measurement, is justified by the increase of the charge carrier energy, which makes the jump or hopping motion through the glass matrix free energy barriers easier [32].

The ac conductivity (σ_{ac}) behavior can be discussed using the jump model [33] assuming that the hopping motion of the ions is not a random process due to the interactions that produce a correlated forward–backward hopping [33]. Thus, in the TET samples, the decrease of the σ_{ac} (Table 1), with the rise of the applied field, should be assigned to the decrease of the free ions number and to the consequent increase in the $LiNbO_3$ crystallites, whose dipoles are difficult to depolarize at room temperature. However, the small fluctuations of the ac activation energy ($E_{a(ac)}$—Table 1), with the increase of the heat-treatment temperature, suggest that

this activation parameter is dominated by the glass matrix rather than by the crystallites characteristics or the mobile ions.

Conclusions

A transparent glass with the composition of $60SiO_2$–$30Li_2O$–$10Nb_2O_5$ (mole %) was prepared by the melt-quenching method. $LiNbO_3$ and $Li_2Si_2O_5$ crystallites were precipitated in the silica glass matrix by heat-treatment at 650 °C. The presence of an electric field, during the heat-treatment, promotes the glass crystallization at lower temperatures (600 °C).

The presence of a white layer, related to surface crystallization, in the anode surface side of the TET samples, shows that the electric field promotes a localized particles precipitation. The rise of the applied field increases the size of the $LiNbO_3$ crystallites, essentially in the sample side in contact with the positive electrode. The Raman spectrum of the TET samples shows that the $LiNbO_3$ formation is privileged in the sample anode zone.

The electrical conduction process of the $60SiO_2$–$30Li_2O$–$10Nb_2O_5$ glass and glass-ceramics, is dominated by the charge carriers number.

Acknowledgements The authors thank to the Fundação para a Ciência e Tecnologia (FCT), for the financial support (SFRH/BD/6314/2001).

References

1. Aboulleil MM, Leonberger FJ (1989) J Am Ceram Soc 72:1311
2. Vogel EM (1989) J Am Ceram Soc 72:719
3. Ding Y, Miura Y, Nakaoka S, Nanba T (1999) J Non-Cryst Solids 259:132
4. Kim JE, Kim SJ, Ohshima K, Hwang YH, Yang YS (2004) Mater Sci Eng A 375–377:1255
5. Weis RS, Gaylord TK (1985) Appl Phys A 37:191
6. Kim HG, Komatsu T, Sato R, Matusita K (1994) J Non-Cryst Solids 162:201
7. Graça MP, Ferreira da Silva MG, Valente MA (2002) Advan Mater Forum I, 161
8. Graça MPF, Valente MA, Ferreira da Silva MG (2003) J Non-Cryst Solids 325: 267
9. Graça MPF, Ferreira da Silva MG, Valente MA (2005) J Non-Cryst Solids 351:2951
10. Martin SW, Angell CA (1986) J Non-Cryst Solids 83:185
11. Macdonald JR (1987) Impedance spectroscopy. John Wiley & Sons, New York
12. Jonscher AK (1983) Dielectric relaxation in solids. Chelsea Dielectrics Press, London
13. Chowdari BVR, Radhakrishnan K (1989) J Non-Cryst Solids 110: 101
14. Kremer F, Schönhals A (2002) Broadband dielectric spectroscopy. Springer, Germany
15. Kim HG, Komatsu T, Sato R, Matusita K (1996) J Mater Sci 31: 2159
16. Fuss T, Ray CS, Kitamura N, Makihara M, Day DE (2003) J Non-Cryst Solids 318: 157
17. Yagi T, Susa M, Nagata K (2003) J Non-Cryst Solids 315:54
18. Navarro JMF (1991) El vidrio. CSIC-Fundación Centro Nacional del Vidrio, Madrid
19. Kusz B, Trzebiatowski K, Barczynski RJ (2003) Solid State Ionics 159:293
20. Zeng HC, Tanaka K, Hiaro K, Soga N (1997) J Non-Cryst Solids 209:112
21. Gerth K, Rüsell C, Kending R, Schleevoigt P, Dunken H (1999) Phys Chem Glasses 40(3):135
22. Nassau K, Wang CA, Grasso M (1978) J Am Ceram Soc 62:503
23. Shibuta N, Horigudhi M, Edahino T (1981) J Non-Cryst Solids 45:115
24. Fukumi K, Sakka S (1988) J Mater Sci 23:2819
25. Umesaki N, Iwamoto N, Tatsumisago M, Minami T (1988) J Non-Cryst Solids 106:77
26. Hirano S, Yogo T, Kikuta K, Isobe Y (1993) J Mater Sci 28: 4188
27. Andrade JS, Pinheiro AG, Vasconcelos IF, Sasaki JM, Paiva JAC, Valente MA, Sombra ASB (1999) J Phys Condens Matter 11: 4451
28. Lipovskii AA, Tagantsev DK, Vetrov, Yanush OV (2003) Opt Mater 21:749
29. Efimov AM (1999) J Non-Cryst Solids 253:95
30. Cardinal T, Fargin E, Le Flem G, Leboiteux S (1997) J Non-Cryst Solids 222:228
31. Koné A, Barrau B, Souquet JL, Ribes M (1979) Mater Res Bull 14:393
32. Matthias BT, Remaika JP (1951) Phys Rev 82 (5):727
33. Cutroni M, Mandanici A (1998) Solid Sate Ionics, 105:149
34. Zhang PX, Mitchell IV, Tong BY, Schultz PJ (1994) Phys Rev B 50(23):17080